Directional Modulation for Enhanced Privacy in Smart Watch Devices

Abel Zandamela, *Graduate Student Member, IEEE*, Nicola Marchetti, *Senior Member, IEEE*, and Adam Narbudowicz, *Senior Member, IEEE*

CONNECT Centre, Trinity College Dublin, The University of Dublin, Dunlop Oriel House, Dublin 2, Ireland

Abstract: This article studies security aspects of data transmission in on-body Internet of Things (IoT) devices through the use of Directional Modulation (DM) from a smart watch integrated antenna. DM is a beamsteering-based Physical Layer Security (PLS) method used to transmit baseband constellations to known secure locations, while simultaneously scrambling them in other directions. However, in the state-of-the-art DM is implemented using large arrays, which are out-sized for many on-body IoT devices. To overcome this challenge, this study proposes multimodal ultra-thin compact antennas suitable for integration into smart watches. These antennas present advanced beamsteering capabilities that allow the implementation of DM from a low-thickness structure of up to 0.57 mm or 1/100th of wavelength at the center operating frequency. Two different DM implementations (simultaneous multiport transmission and an energy-efficient single-port transmission) are tested using a multi-layer phantom. Overall, secure steerable transmissions are realized, and experimental verifications are carried out to validate the proposed concept. Ultimately, this article demonstrates the feasibility of applying new energy-efficient and low-cost security techniques to enhance the privacy of resource-constrained IoT devices.

Index Terms: Directional modulation, physical layer security, beamsteering antennas, low-profile antennas, smart watch, on-body antennas, wearable IoT devices.

1. Introduction

While still being a relatively nascent field, Physical Layer Security (PLS) allows to complement the privacy of many cutting-edge wireless systems like Multiple-Input Multiple-Output (MIMO), Internet of Things (IoT), and others [1]–[3]. PLS techniques can provide additional protection against eavesdroppers by exploiting the physical characteristics of the wireless propagation channel, e.g. noise, fading, and interference. A potential area that can benefit from those methods is the growing field of wearable devices, where classical cryptography may be unsuitable to implement due to tight energy and low processing power constraints [4].

Wearables are becoming indispensable to many modern applications, i.e. health care and IoT systems [4]–[6]; however, they are susceptible to eavesdropping as the data transmission is done in an open wireless medium. The security issues are especially challenging for wearables as they also need to be compact to fit into body parts, e.g. human wrist and foot; therefore, small and low-profile antennas are desirable for integration into wearables. In addition, antennas for wearables need to account for coupling effects and efficiency deterioration due to the lossy human body [7]–[9]. Moreover, beamsteering is desirable, as this can allow providing additional security through PLS methods like Directional Modulation (DM). The DM technique can enhance the privacy of wireless systems by optimizing the beamsteering of arrays to transfer baseband constellations symbols to a pre-specified secure direction while simultaneously distorting the same constellations in all other directions [10], [11].

To address wearable devices' security issues, this work introduces for the first time the use of DM from an ultra-thin smart watch antenna. The work also proposes a general framework for how DM can be used in compact IoT devices. Then, a discussion of the proposed multimodal antenna is presented, and beamsteering characteristics are demonstrated across the entire azimuth plane using a model of only 0.024λ ($1.34\,\mathrm{mm}$) thickness, with further tuning demonstrated for $0.57\,\mathrm{mm}$ or 0.01λ (where λ is the wavelength at the center operating frequency, i.e. $5.57\,\mathrm{GHz}$). Next, we

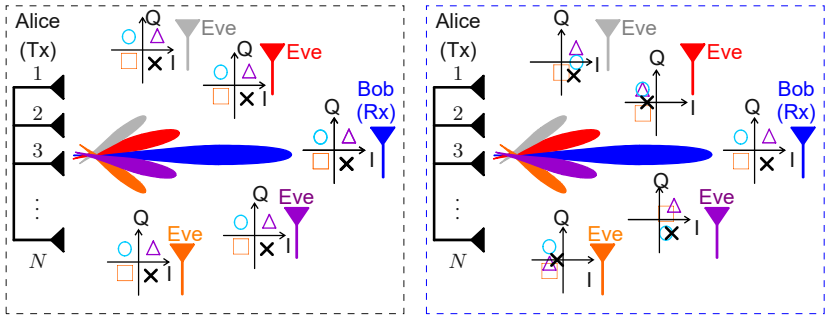

Fig. 1. Visualization of the traditional beamsteering (a) and the DM method (b). The transmitter (Tx) Alice is an array comprising N elements, Bob is the direction of the LU, and eavesdroppers (Eves) are located in different directions. Note that in the traditional beamsteering, the IQ constellations are the same in all directions, while they are only decipherable in the Bob direction for the DM approach.

evaluate the electromagnetic field exposure of the antenna by computing the Specific Absorption Rate (SAR) following the Federal Communications Commission (FCC) recommended setups for both the wrist-worn case and next-to-the-mouth conditions. Lastly, two DM implementations are tested in free space and with a multi-layer phantom. The first DM scheme requires simultaneous multiport activation with artificial noise, while the second DM approach only needs a single port activation without excessive artificial noise. The performance of both methods is investigated using full-wave simulations and validated through anechoic chamber measurements.

2. Directional Modulation

In traditional beamsteering, data transmission is done with the maximum power in the direction of the legitimate user (LU), with the power in eavesdroppers' locations being as low as possible. The baseband constellations, i.e. the complex values in the In-phase Quadrature (IQ) plane, are the same for all transmitting directions of the antenna as shown in Fig. 1a. This means that the difference between the directions are power levels and phase differences created by different propagation paths - both can be corrected by a reasonably advanced eavesdropper [2]. To enhance the secrecy, the DM technique preserves the original QAM constellation in the desired LU direction while, at the same time, it spatially scrambles them in all other directions (see Fig. 1b).

Babakhani et al. introduced in [12] the near-field direct antenna modulation using a driven dipole combined with passive reflectors. In [10], Daly and Bernhard demonstrated a similar secure modulation approach using a four-element reconfigurable array. Hong et al. presented in [13] a dual-beam DM method; unlike [10] and [12], where the same antennas transmit the IQ patterns, in this approach, different antennas transmit the IQ patterns. Further research on DM is presented in [11], where Ding and Fusco introduced an orthogonal vector approach for DM transmitter synthesis; in [14], Ding and Fusco also introduced a new type of DM transmitter based on retro-directive arrays, where the injected orthogonal interference is not dependent on the pre-selected secure direction. Other contributions in the field are presented e.g. in [15]–[31], phased arrays are used in [15]; switched antenna arrays are discussed in [16]–[18]; multi-user MIMO DM systems are studied in [19], [21], [23]; time-modulated arrays are investigated in [20] and [26]; hybrid MIMO phased arrays are studied for mm-Wave communication systems in [25]; and dynamic multi-beam DM using random changes of the artificial noise vector at the symbol rate is proposed in [22].

3. Challenges and Limitations of DM for Small IoT Devices

Most DM schemes discussed above are implemented using classical arrays. Since those typically require $\lambda/2$ inter-element spacing, they are challenging to use in wearable IoT systems. To address these issues, in this Section, we first discuss MIMO antennas proposed for pattern diversity

in smart watches. Then, a review of DM implementations using compact antennas and recent advances in energy-efficient DM techniques are presented.

3.1. MIMO Antennas for Smart Watch Devices

In recent years, different compact antennas have been proposed for smart watch devices, e.g. in [32]–[46]. Among those, MIMO designs have been studied in [41]–[46]. Wen et al. [44] exploited the theory of characteristics mode analysis to design a $7\,\mathrm{mm}$ thick 2-port MIMO antenna, with bidirectional and omnidirectional patterns, where the gain and efficiency drop from $3.5\,\mathrm{dBi}$ and 75% (free space) to $2\,\mathrm{dBi}$ and 42% (with hand-phantom). In [46], Liao et al. investigate a $8\,\mathrm{mm}$ thick L-shaped slot and loop-based MIMO antenna, covering five different bands, with an efficiency $> 25\%$ when tested on a hand phantom. Other MIMO smart watch designs are discussed e.g.: in [41] (2 port MIMO design based on a folded monopole with a thickness of $5\,\mathrm{mm}$); in [42] (a $5.4\,\mathrm{mm}$ thick 2 port MIMO based on the inverted-F antenna); [43] (a $5\,\mathrm{mm}$ thick 3 port multiband MIMO design) and in [45] ($7.5\,\mathrm{mm}$ thick 2 port MIMO based on an annular ring).

While the above works show significant improvements in their pattern diversity and other antenna performance, they still have a large profile. More importantly, their beamforming performance is limited for DM implementation (as the desired secure direction of the LU can be in any direction in the 3D space). This means that the beamforming of the antenna should allow the main beam to be pointed at the LU and maintain the true constellation in that direction (see Fig. 1b), while the signal in other directions is weak and the constellation symbols are distorted. However, such performance cannot be realized using the beamforming of the works discussed above.

3.2. DM from Compact Antennas and Energy Efficient DM Schemes

In recent years, only a few works have proposed DM schemes in small IoT devices. Narbudowicz et al. [27] introduced a compact DM system using a dual-mode antenna of $\lambda/2$ diameter and 0.31λ profile. Parron et al. [28] proposed a four-mode stacked patch design of diameter 0.7λ and 0.05λ profile. Although a low-profile design is achieved in [28], high-side lobes are present, which can compromise the security of the transmitted data. Moreover, the solution uses a stacked patch approach, and similarly to [27], such designs are challenging for smart watch devices' packaging. The work in [29] proposes a DM method using a $3\lambda/2$ switched dipole antenna; however, it is still too bulky for integration in smart watch devices. Recently in [30], we proposed a five-mode antenna (0.65λ diameter and 0.19λ profile), capable of unique steerable DM transmissions without high side lobes. However, the profile is still relatively high for wrist-wearable IoT devices. In addition, like [27], [28], it is a stacked patch antenna, which presents challenges for smart watch packaging, as typically very low-profile antennas are desirable to allow for placement of other smart watch components such as the battery, LCD display, heart rate monitor and others.

A few approaches have been proposed to improve the energy efficiency of DM techniques e.g.: RF power amplifiers efficiency [47]; power efficiency and security of QAM and APSK DM systems [48]; time-modulated phased arrays requiring only a single active RF-chain [49]; and reconfigurable power dividers [50]. While the above methods present significant breakthroughs, their implementation for small IoT devices is not feasible due to the higher computational demands and the requirement of sophisticated switching sequences with careful synchronization. In our recent work [31], we propose a simple single active RF-chain DM scheme, where the switching sequence can be fully random and independent of the direction of the LU. Nevertheless, the implementation uses a 5-element array, which is still a large diameter and profile for smart watch device packaging.

4. Ultra-thin Multimodal Antennas for DM in Smart Watches

The proposed multimodal antenna is shown in Fig. 2 and operates near $5.57\,\mathrm{GHz}$, is $1.34\,\mathrm{mm}$ thick with $33\,\mathrm{mm}$ diameter ($0.61\lambda \times 0.61\lambda \times 0.024\lambda$). The design uses a single layer of Rogers TMM6 substrate ($\epsilon_r = 6$, $tan\delta = 0.0023$) and comprises two concentric shorted ring structures fed using three ports to excite different orthogonal modes. The inner ring is fed using P1 and

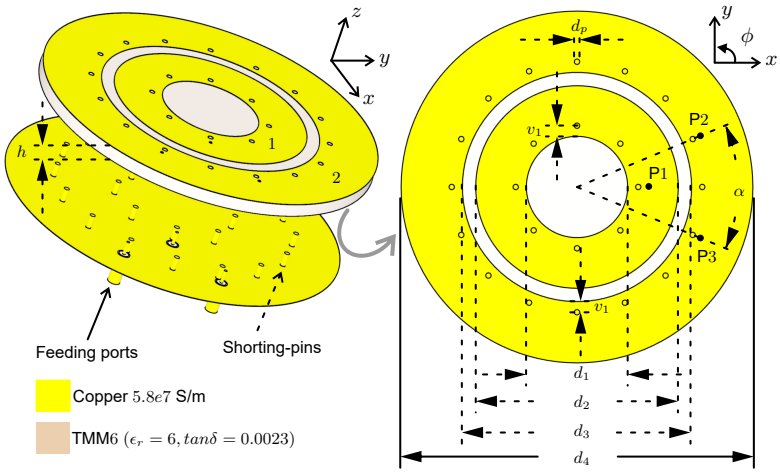

Fig. 2. Proposed antenna, design A (not to scale); dimensions (all in mm): $h = 1.27$, $d_1 = 10$, $d_2 = 18$, $d_3 = 21.5$, $d_4 = 33$, $d_p = 0.5$, $v_1 = 1$, $\alpha = 45°(135°)$; feed points: P1 $= 7$, P2 $=$ P3 $= 12.5$.

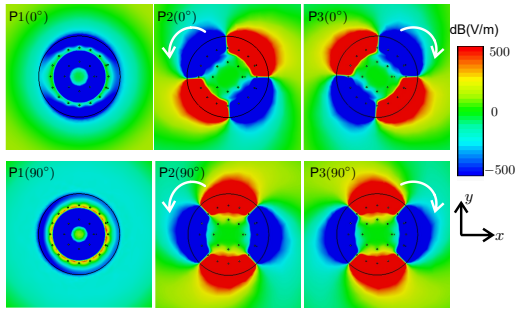

Fig. 3. E-field distribution ($z-$components) for each port of the proposed multimodal ultra-thin antenna: (top) $0°$ phase; and (bottom) $90°$ phase.

includes eight shorting pins rotated by $45°$ with respect to the center. Due to the inductance of the pins, an increase in the resonance frequency is observed compared to the case without the pins. The outer ring is fed using P2 and P3, it includes 16 pins rotated by $22.5°$ with respect to the center. In both rings, the pins are placed at a distance v_1 from the inner radius. Note that good isolation and frequency tuning can be obtained by controlling the total number of pins and the value v_1; in general, the higher the number of pins and v_1, the larger frequency shift is obtained. The parameter v_1 is optimized to $1\,\mathrm{mm}$ for both rings, and the number of pins is selected taking into account the symmetry between the feeding ports. The antenna is simulated in free space using a finite element method-based 3D full-wave solver. The electric field distribution for each port is shown in Fig. 3. It is seen that P1 excites a monopolar-like pattern, while P2 and P3 excite two orthogonal modes of the same order; the mode purity of each excited pattern compared to the respective ideal spherical mode pattern is above 98% for all the ports.

Next, a hand phantom based on the computed tomography results of [51] is used to evaluate the performance on the user's wrist. The phantom comprises four layers (see Fig. 4), with the skin and the fat layers occupying 15% of the total volume; the muscle layer occupies 72.1%, and the bone layer occupies 12.9%. The respective dielectric properties of each layer are obtained from [52]. To evaluate the antenna performance in a realistic scenario, a pig's foot of length $205\,\mathrm{mm}$ is used as the phantom. The manufactured prototype is shown in Fig. 4; and in both cases (simulated and measured), the antenna is placed in direct contact (i.e. $0\,\mathrm{mm}$ separation) with either the skin layer of the phantom or the pigs' foot. Note that this setup assumes the worst-case scenario

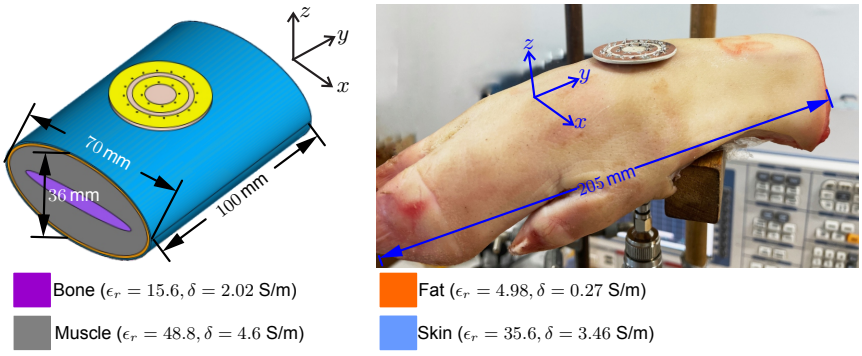

Fig. 4. Proposed setups (not to scale): users' wrist scenario where the antenna is placed in direct contact with the skin layer of the phantom (left); and measurement setup using pigs' foot of length $205\,\mathrm{mm}$, with width and thickness of approximately $50\,\mathrm{mm}$ (right).

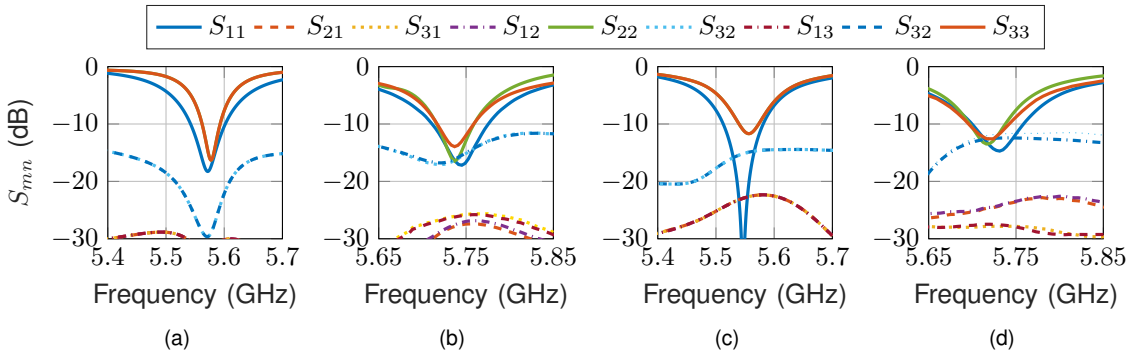

Fig. 5. S-parameters results: (a) simulated free space; (b) measured free space; (c) simulated with hand-phantom; and (d) measured with hand-phantom.

(antenna in direct contact with the lossy hand phantom or pigs' foot); the implication is that a much larger efficiency drop will occur in our proposed setup due to the antenna's close proximity to the phantom. However, its ultra-thin properties allow placement at different heights inside the smart watch housing.

The antenna offers good isolation characteristics owing to the orthogonality of the excited modes. The isolation is better than $29\,\mathrm{dB}$ (free space, Fig. 5a), and $15\,\mathrm{dB}$ (including phantom, Fig. 5c) for the simulated case. For the measured case the isolation is better than $15\,\mathrm{dB}$ (free space, Fig. 5b) and $12\,\mathrm{dB}$ (including phantom, Fig. 5d). Note that a frequency shift is observed between the simulated and measured cases in free space, from $5.57\,\mathrm{GHz}$ (simulations) to $5.73\,\mathrm{GHz}$ (measurements); this is most likely due to the combined effect of the substrate permittivity and fabrication tolerances. In addition, the setup with body phantom shows a small shift toward lower frequencies from $5.73\,\mathrm{GHz}$ (Fig. 5b) to $5.71\,\mathrm{GHz}$(Fig. 5d). At the center frequency of each case, the antenna total efficiency in free space is 76% (for P1), 57% (for P2 and P3); changing to 52% (for P1), and 41% (for P2 and P3), when including the phantom. The measured $-10\,\mathrm{dB}$ impedance bandwidth is $41.4\,\mathrm{MHz}$ (free space) and $37.6\,\mathrm{MHz}$ (including the phantom).

Lastly, to test the effect of different smart watch components, lossy metals with a dielectric shell ($\epsilon_r = 1.5$) are used to simulate a $0.7\,\mathrm{mm}$ thick printed circuit board assembly (PCBA) and a $3\,\mathrm{mm}$ thick battery (see Fig. 6a). The antenna, PCBA, and battery are placed inside a plastic case, where a $1\,\mathrm{mm}$ gap between all the components and the housing is introduced. A plastic band of width $20\,\mathrm{mm}$, with $14\,\mathrm{mm}$ rectangular end strips is connected at two opposite sides of the plastic housing (see Fig. 6a). The S-parameters results are shown in Fig. 6b. For this case, P2 and P3 have a small downward frequency shift, which, however, can be easily tuned, depending on the final design of the commercial product. Nevertheless, the $\vec{E}$-field patterns have similar characteristics

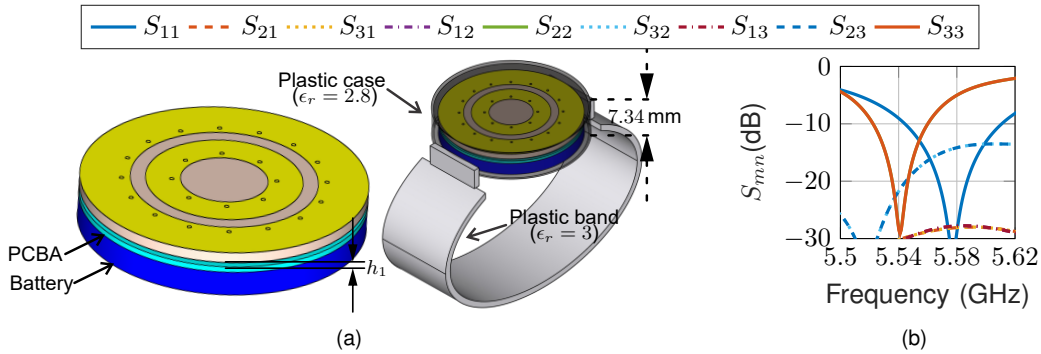

Fig. 6. Antenna with smart watch components: (a) antenna tested with PCBA, battery, plastic housing of $7.34\,\mathrm{mm}$ thickness and a plastic wristband, where $h_1 = 0.5\,\mathrm{mm}$; (b) S-parameters results.

with the free space results, and an overlap $-10\,\mathrm{dB}$ bandwidth of $14\,\mathrm{MHz}$ is realized.

4.1. Antenna Pattern Performance on Gustav Voxel Model and SAR Analysis

To test the antenna pattern on a realistic human model, the multimodal design was simulated with the CST Studio Suite Gustav voxel model. The patterns were tested in two different setups: hand along the body (Fig. 7a) and the elevated hand case (Fig. 7b). It can be seen that small pattern deformities and deeps are present, especially for directions that lie along the hands' length. Such deformities are mostly due to the voxel model electromagnetic absorption and reflections from its surface. Note that those small deeps occur mostly around the $+y$ direction, i.e. towards the voxel model. Because it is often desired to radiate away from the body, the beamsteering towards the $-y$ direction is still realized. In general, all three ports still present the required pattern properties to allow for good beamforming characteristics.

Because the antenna is proposed to operate on a human wrist, we analyzed the electromagnetic field exposure by computing the Specific Absorption Rate (SAR). The calculations were done following the FCC guidelines under two conditions: wrist-worn case, where the device is placed in direct contact with a block filled with human hand tissue ($\epsilon_r = 21.1$, $\delta = 0.52$, and $\rho = 1000\,\mathrm{kg/m^3}$), and averaged in $10\,\mathrm{g}$; the second case is the next-to-the-mouth one, with the device placed at a

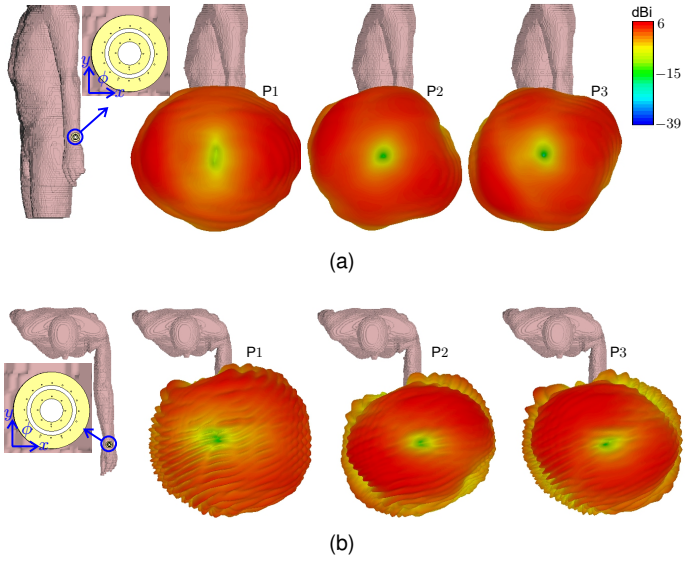

Fig. 7. Antenna directivity patterns on Gustav voxel model: (a) setup with the hand along the body; and (b) setup with the elevated hand.

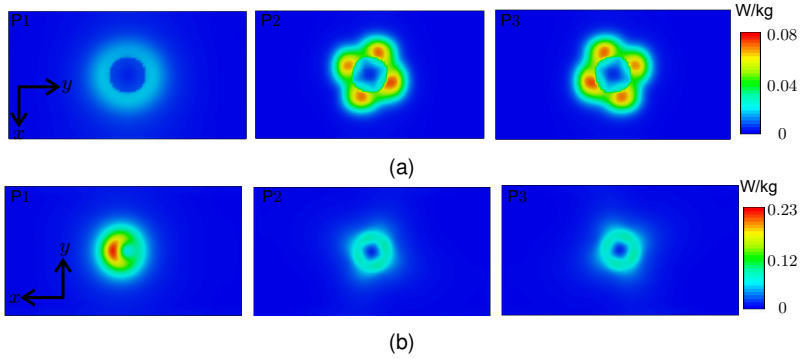

Fig. 8. Antenna SAR results following FCC guidelines: (a) wrist-worn setup; and (b) next-to-the-mouth setup.

$10\,\mathrm{mm}$ distance from a block filled with human head tissue ($\epsilon_r = 35.1$, $\delta = 5.3$, and $\rho = 1000\,\mathrm{kg/m^3}$) and $1\,\mathrm{g}$ averaging. An input power of $10\,\mathrm{mW}$ is used, and for the wrist-worn condition, the largest value of SAR between all the ports is $0.073\,\mathrm{W/kg}$ (see Fig. 8a), which is still well below the FCC limits of $4\,\mathrm{W/kg}$. For the next-to-the-mouth condition the largest SAR is $0.22\,\mathrm{W/kg}$ (see Fig. 8b), also staying well below the $1.6\,\mathrm{W/kg}$ limit.

4.2. Calculated Beamsteering Results

To realize beamsteering within size-constrained space, the proposed multimodal ultra-thin antenna exploits the different phase variations of each radiated mode – the method is detailed in [53] – and it is based on the fact that the $\vec{E}$-field at a large distance ($kr \to \infty$) can be expressed as a weighted sum of the far-field spherical wave pattern functions $\vec{K}_{smn}$ defined as [54]

$$\vec{E}(r,\theta,\phi) = \sqrt{\eta}\frac{k}{\sqrt{4\pi}}\frac{e^{ikr}}{kr}\sum_{smn} Q_{smn}\vec{K}_{smn}(\theta,\phi) \tag{1}$$

where η is the specific impedance of the medium, $k = 2\pi/\lambda$ is the specific wavenumber, and Q_{smn} are the spherical modes' coefficients; s represents the polarization, where for TM-modes $s = 1$ corresponds to the $\vec{H}$-fields and $s = 2$ represents the $\vec{E}$-fields, and the opposite is true for the TE-modes. The indices (m, n), with $|m| \leq n$, indicate the azimuthal phase change and the order of the spherical mode, respectively. The spherical wave functions $\vec{K}_{smn}(\theta,\phi)$ are power-normalized dimensionless solutions of the vector wave equation. For the proposed beamsteering principle, the modes of interest are of type $s = 1$, and assuming e^{-iwt} time dependency, they are given as

$$\vec{K}_{1mn}(\theta,\phi) = \frac{1}{\sqrt{2\pi}}\frac{1}{\sqrt{n(n+1)}}\left(-\frac{m}{|m|}\right)^m \mathrm{e}^{im\phi}\left\{\frac{im\bar{P}_n^{|m|}(\cos\theta)}{\sin\theta}\vec{e}_\theta - \frac{d\bar{P}_n^{|m|}(\cos\theta)}{d\theta}\vec{e}_\phi\right\} \tag{2}$$

where $\bar{P}_n^{|m|}\cos\theta$ is the normalized associated Legendre function. To realize the proposed beamsteering, the $\vec{K}_{1mn}$ modes can have different order, i.e. $n = 1, 2, 3, \cdots N$. Next, the order of the modes excited by the largest ring is assumed to be the highest order that can be excited in the structure, then all the lowest-order modes are also excited using the remaining rings. All the modes are required to be omnidirectional with different azimuthal phase variations m. From (2), the modes generated by each port of the proposed antenna are shown in Fig. 10b and can be classified as P1 $\to \vec{K}_{1,0,1}$, P2 $\to \vec{K}_{1,-2,2}$, and P3 $\to \vec{K}_{1,+2,2}$. It is seen that the phase of the pattern radiated by ring-1 is monopole-like, i.e. with constant phase across the entire azimuth plane ($m = 0$), while the phase changes twice for ring-2 ($m = \pm 2$). Note that the phases of ring-2 change in two opposing directions, i.e. the "$+$" sign indicate the clockwise direction, and the "$-$" sign is the counter-clockwise direction. These properties are exploited to create constructive interference in desired directions by means of phase control, allowing for beamsteering while using a compact size with a thickness suitable for smart watch device packaging.

To evaluate the proposed beamsteering principle, measurements were performed in an anechoic chamber both in free space and with the phantom. The measurement setup is shown

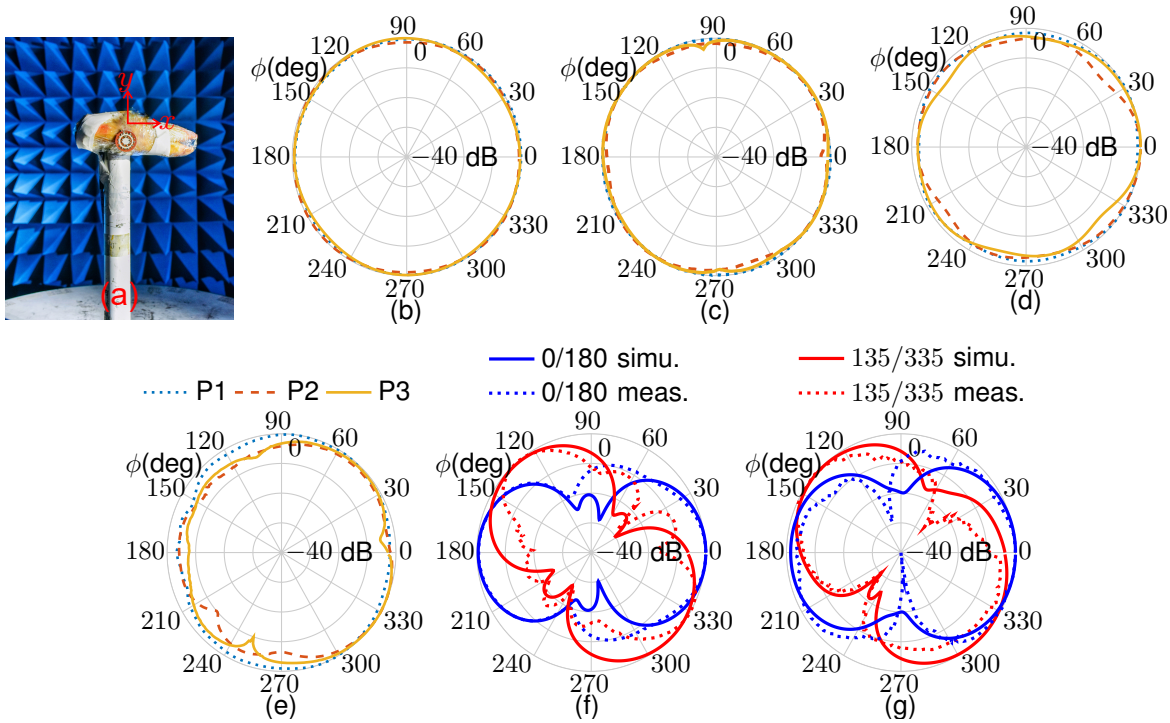

Fig. 9. Normalized patterns: (a) anechoic chamber measurements setup with the pigs' foot; (b) free space simulated results; (c) free space measured results; (d) simulations with the phantom; (e) measurements with phantom; (f) free space beamsteering; and (g) beamsteering results with phantom.

TABLE I
Amplitude and Phase Configuration of the Generated Beams

Beam direction	P1 (A_{inp})	P1 (Δ_{ph})	P2 (A_{inp})	P2 (Δ_{ph})	P3 (A_{inp})	P3 (Δ_{ph})
$0°/180°$ (free space)	1	$0°$	1	$68°$	1	$-23°$
$135°/315°$ (free space)	1	$0°$	1	$-23°$	1	$70°$
$0°/180°$ (phantom)	1	$0°$	1	$33°$	1	$33°$
$135°/315°$ (phantom)	1	$0°$	1	$-55°$	1	$-245°$

in Fig. 9a. The free space patterns for each port are shown in Fig. 9b (simulated case) and Fig. 9c (measured case); it is seen that a good agreement is achieved with both cases showing omnidirectional patterns for each antenna port. Fig. 9d shows the simulated patterns with the phantom, and their counterpart measured results are shown in Fig. 9e; it is observed that some shouldering and deeps are present in the measured case. This discrepancy may be due to the reflections of the antenna holder and other pigs' foot assembly components during measurements. The beamsteering performance in free space is shown in Fig. 9f, and the results, including the phantom, are shown in Fig. 9g. It is seen that for both cases, a bidirectional pattern is realized, and the desired main beam directions are in good agreement with the simulated cases. The input amplitude (A_{inp}) and phase shift (Δ_{ph}) for each port of the generated beams are shown in Table I.

4.3. Tuning Capabilities of the Ultra-thin Multimodal Design

The proposed beamsteering principle allows for a wide tuning range of the antenna parameters. To highlight such design flexibility, Fig. 10a (left) shows a variation of the antenna shown in Fig. 2. The new antenna (design B) uses the same diameter as design A (Fig. 2) but is loaded with TMM10 substrate, with $\epsilon_r = 10$ (as compared to design A, with TMM6 and $\epsilon_r = 6$). This allows further miniaturization as the center frequency shifts from $5.57\,\mathrm{GHz}$ (design A) to $4.48\,\mathrm{GHz}$ (design

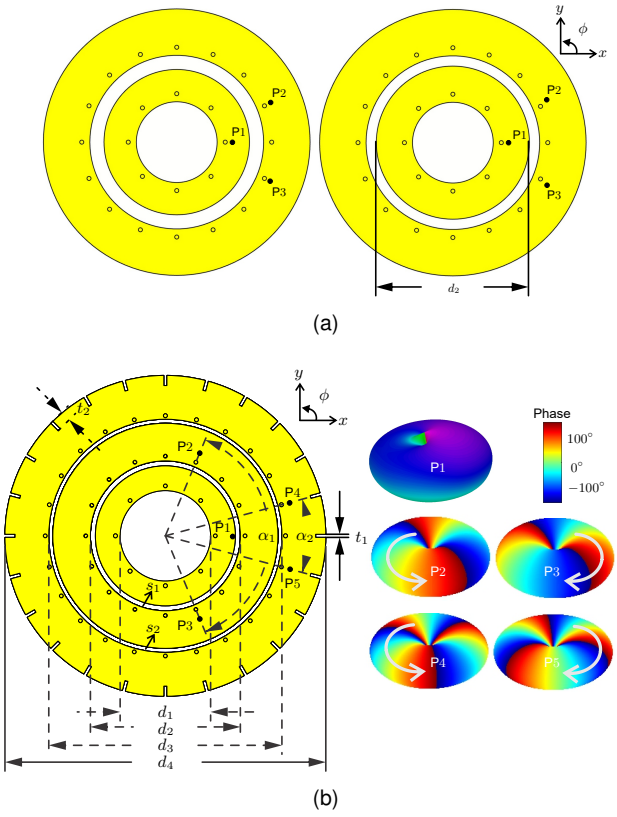

Fig. 10. Multimodal antennas (not to scale), all dimensions in mm: (a) left image shows design B (P1 $=$ 7, P2 $=$P3 $=$ 12.25) and the right image shows design C (P1 $=$ 7, P2 $=$P3 $=$ 12.75, $d_2 = 18.95$); and (b) left image shows design D [$d_1 = 11.56$, $d_2 = 19.16$, $d_3 = 29.8$, $d_4 = 41$, $s_1 = 0.64$, $s_2 = 0.52$, $t_1 = 0.4$, $t_2 = 1.3$, $\alpha_1 = 135°(45°)$, $\alpha_2 = 30°(90°)$, P1 $= 8.6$, P2 $= 11.5$, P3 $= 11.5$, P4 $= 16.5$, and P5 $= 16.5$, the remainder of the dimensions follow design A]; the right image shows the phase of the radiation patterns of the proposed designs.

TABLE II
Analysis of the Tuning Capabilities of the Proposed Principle

Design	f_0 (GHz)	Size	ϵ_r	S_{mn} (dB)	-10 dB IBW(MHz)	Tot. Eff. (%)
A	5.57	$0.61\lambda \times 0.61\lambda \times 0.024\lambda$	6	> 29	31	57
B	4.48	$0.49\lambda \times 0.49\lambda \times 0.02\lambda$	10	> 25	7	36.5
C	5.51	$0.6\lambda \times 0.6\lambda \times 0.01\lambda$	6	> 25	25	26.6
D	5.77	$0.78\lambda \times 0.78\lambda \times 0.02\lambda$	6	> 21.6	25	45.5

B). Note that due to miniaturization, the total efficiency drops to around 36.5% (57% in design A), and the isolation is better than $25\,\mathrm{dB}$. The thickness of the substrate material of the antenna can also be tuned as shown in Fig. 10a (right), i.e. design C, which uses a substrate thickness of $0.5\,\mathrm{mm}$, and the total antenna thickness is then $0.57\,\mathrm{mm}$.

Fig. 10b shows the design D, which is capable of unidirectional beamsteering around the azimuth plane. This is achieved by adding a new ring exciting $\vec{K}_{1,-3,3}$, and $\vec{K}_{1,+3,3}$ modes; therefore, a total of five modes are combined for beamsteering, i.e. $m = 0$ (constant-phase), $m = \pm 2$ (dual azimuthal-phase change), and $m = \pm 3$ (triple azimuthal-phase change). Note that the 3-ring antenna uses the lowest number of modes that can allow for unidirectional beamsteering around the desired plane. Lastly, a comparison of the four different designs is shown in Table II. Note that because of the good trade-off offered by design A (in terms of size, efficiency, and beamsteering), all the DM results discussed in the following Section are calculated using this model.

5. Directional Modulation from Ultra-thin Multimodal Antennas

5.1. Proposed Directional Modulation Schemes

Two DM schemes are studied with the proposed antenna: in scheme 1, all the complex patterns generated by exciting each port are used as DM weights, and artificial noise is added to scramble the IQ constellations in all undesired directions [53]. In scheme 2, only the complex patterns generated by a single port are used, with no excessive artificial noise in undesired directions [31].

Without loss of generality, we will use QPSK, and it is assumed that the transmitted signal propagates through a Line-of-Sight channel, and the DM schemes are evaluated as follows:

1) First, far-field results of design A (Fig. 2) are obtained from a 3D full-wave solver or trough anechoic chamber measurements. The complex patterns of the antenna are extracted in free space, including the wrist phantom or pigs' foot (see Fig. 5).
2) The DM transmissions are studied for the entire azimuth plane; i.e. the elevation angle is fixed at $\theta = 90°$, with the azimuth angles ϕ having a $1°$ resolution.
3) Next, DM schemes are implemented using MATLAB; a symbol is modulated using QPSK, and the resulting complex data symbol is denoted as $d \in \{1; j; -1; -j\}$.
4) For scheme 1:
   - A random complex vector $\vec{s'}$ comprised of $\frac{N}{2}$ elements (where N is the total number of ports in the antenna) is drawn with uniform distribution from $[-1, 1]$ and $[-j, j]$.
   - Next, to scatter the constellation symbols, a vector $\vec{s}$ comprising N-elements is obtained from a random permutation of the elements of the vector $\vec{s'}$ and its negation, giving $\sum_{n=0}^{N-1} \vec{s}_n = 0$, ensuring random noise cancellation in the desired secure direction. In addition, the permutation avoids any regularity that can be exploited by eavesdroppers, as random values will be assigned to different antenna ports.
   - Next, the vector $\vec{m}$ is formed by adding the modulated symbol d to each element of $\vec{s}$.
   - Then, the transmitted signal pre-coding is applied through zero-forcing. Each element is then communicated by the complex pattern excited by each respective antenna port.
   - Lastly, Additive White Gaussian Noise (AWGN) is added at the receiver and is assumed to be independent at each location.
5) For scheme 2:
   - First, a random number generator is used to select the reference port to establish the handshake; this step should be done as often as possible for increased security.
   - Then, phase compensation is added in the desired direction of the legitimate user to account for phase variation when switching between antenna ports, while random phase changes are observed in any other direction.
   - AWGN is added at the receiver and is assumed to be independent in each direction.
6) Both DM schemes are tested using 10^5 transmitted symbols and a Signal to Noise Ratio (SNR) of $12\,\mathrm{dB}$, and the performance is evaluated through Bit Error Rate (BER) calculations.

5.2. Directional Modulation Performance

Fig. 11a shows the DM concept for the users' wrist scenario, where the IQ constellations are only decipherable in the Bob direction.

Fig. 11b - Fig. 11e show the BER performance for Schemes 1 and 2 at the center frequency of each case. In all four cases, the transmissions are tested for two different directions of the LU: $\phi_{Bob} = 45°$, and $\phi_{Bob} = 135°$. The DM performance in free space is shown in Fig. 11b (for $\phi_{Bob} = 45°$) and Fig. 11c (for $\phi_{Bob} = 135°$). It is seen that very low BER values are realized at the desired LU directions for both schemes; however, it should be noted that due to the bidirectional beamsteering of design A, a second direction with low BER values is observed at $\phi_{Bob} + 180°$. Nevertheless, design D (Fig. 10b) can be used for applications requiring unique secure transmissions across the entire azimuth plane. The DM performance for the users' wrist scenario is shown in Fig. 11d (for $\phi_{Bob} = 45°$) and Fig. 11e (for $\phi_{Bob} = 135°$); good agreement is also obtained with very low BER values at the desired LU directions.

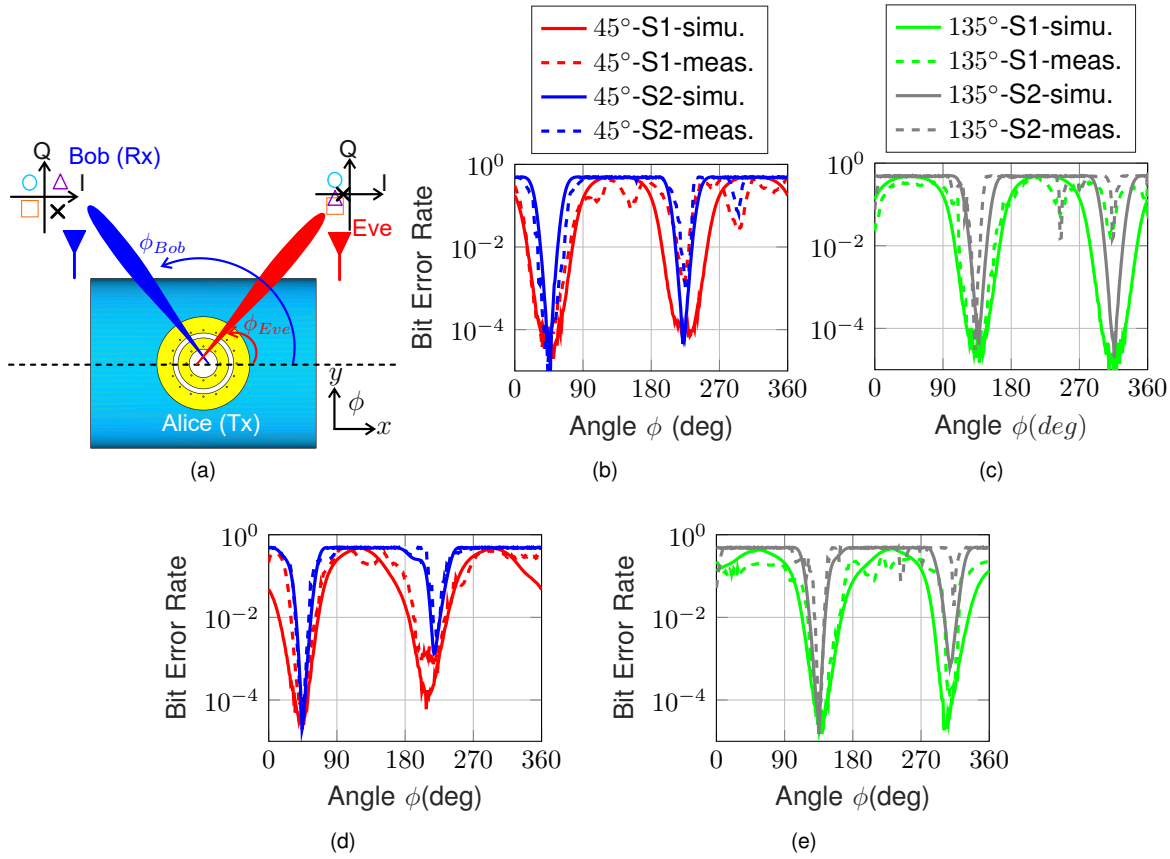

Fig. 11. BER calculations: (a) proposed DM scheme for users' wrist scenario, where the multimodal antenna (Alice) is the transmitter, the desired secure transmission direction is the Bob direction (ϕ_{Bob}), while eavesdropper (Eve) are present in the azimuth plane ($xy-$plane), and S1 represents Scheme-1, while S2 is Scheme-2; (b) free space DM results for $12\,\mathrm{dB}$ SNR scenario for $\phi_{Bob} = 45°$, simulated case (solid lines) and measured case (dashed lines); (c) free space results for $\phi_{Bob} = 135°$; (d) DM results for the users' wrist scenario for $\phi_{Bob} = 45°$; and (e) users' wrist scenario for $\phi_{Bob} = 135°$.

For the free space case the largest BER$< 10^{-2}$ beamwidth for the investigated LU directions is $60°$ for scheme 1, and $13°$ for scheme 2. These values change to $53°$ for scheme 1 and $14°$ for scheme 2 when evaluated in the users' wrist scenario. Overall, these results demonstrate that in all the investigated cases, the BER beamwidth for scheme 2 is much narrower (approximately four times narrower) compared to the beamwidth obtained with scheme 1. This translates into increased privacy as the decipherable IQ constellations are transmitted in a much smaller region, limiting the possibility of eavesdroppers to access the information. This performance also highlights that secure transmissions are realized without simultaneous activation of multiple ports, which reduces the energy consumption in smart watches, as only a single port is active at a time. The proposed techniques are therefore expected to bridge the current gap between the security issues of on-body wearables IoT devices and low-computational power requirements, e.g. in off-body communications of many emerging applications like the Internet of Medical Things.

Conclusion

This article addressed the directional modulation from resource-constrained wrist-worn IoT devices. Firstly, it provided an overview of the directional modulation physical layer security (PLS) technique. Then it proposed a compact and IoT-compatible solution that allows for the first time to effectively use such techniques from smart watch devices. This functionality was made possible by

recent advances in ultra-thin antenna technology, integrated into constrained spaces and operating efficiently in proximity to the human body. By exploiting the phase characteristics of the antenna, one can realize beamsteering properties to cover the entire azimuth plane with a low-profile structure of $1.34\,\mathrm{mm}$, with further tuning capability to $0.57\,\mathrm{mm}$. This beamsteering capability is subsequently used to execute the directional modulation security scheme. The technique further addressed current challenges posed by smart watch energy constraints by enabling the implementation of an energy-efficient single-RF-chain directional modulation scheme. The proposed work can significantly contribute to the new area of PLS for wearable IoT devices, thanks to its capability for miniaturization and the use of single-RF-chain techniques.

Acknowledgements

This publication has emanated from research conducted with the financial support of Science Foundation Ireland under Grant number 18/SIRG/5612.

References

[1] X. Chen *et al.*, "A Survey on Multiple-Antenna Techniques for Physical Layer Security," *IEEE Com. Surveys & Tutorials*, vol. 19, no. 2, pp. 1027–1053, 2017.
[2] D. Trung, Z. Xiangyun, and H. V. Poor, *Trusted Communications with Physical Layer Security for 5G and Beyond*. Institution of Engineering and Technology, 2018.
[3] Z. Wei *et al.*, "Energy- and Cost-Efficient Physical Layer Security in the Era of IoT: The Role of Interference," *IEEE Com. Mag.*, vol. 58, no. 4, pp. 81–87, 2020.
[4] S. Seneviratne *et al.*, "A Survey of Wearable Devices and Challenges," *IEEE Com. Surveys & Tutorials*, vol. 19, no. 4, pp. 2573–2620, 2017.
[5] J. W. Kim *et al.*, "Collecting Health Lifelog Data From Smartwatch Users in a Privacy-Preserving Manner," *IEEE Trans. Consumer Electron.*, vol. 65, no. 3, pp. 369–378, 2019.
[6] Y. Qadri *et al.*, "The Future of Healthcare Internet of Things: A Survey of Emerging Technologies," *IEEE Com. Surveys & Tutorials*, vol. 22, no. 2, pp. 1121–1167, 2020.
[7] G. A. Conway and W. G. Scanlon, "Antennas for Over-Body-Surface Communication at 2.45 GHz," *IEEE Trans. Antennas. Propag.*, vol. 57, no. 4, pp. 844–855, 2009.
[8] F. Merli *et al.*, "Design, Realization and Measurements of a Miniature Antenna for Implantable Wireless Communication Systems," *IEEE Trans. Antennas. Propag.*, vol. 59, no. 10, pp. 3544–3555, 2011.
[9] D. Gasperini *et al.*, "Matching Layer Design for Far-Field and Near-Field Penetration Into a Multilayered Lossy Media [Bioelectromagnetics]," *IEEE Antennas Propagat. Mag.*, vol. 64, no. 5, pp. 86–96, 2022.
[10] M. P. Daly and J. T. Bernhard, "Beamsteering in Pattern Reconfigurable Arrays Using Directional Modulation," *IEEE Trans. Antennas. Propag.*, vol. 58, no. 7, pp. 2259–2265, 2010.
[11] Y. Ding and V. F. Fusco, "A Vector Approach for the Analysis and Synthesis of Directional Modulation Transmitters," *IEEE Trans. Antennas. Propag.*, vol. 62, no. 1, pp. 361–370, 2014.
[12] A. Babakhani, D. B. Rutledge, and A. Hajimiri, "Transmitter Architectures Based on Near-Field Direct Antenna Modulation," *IEEE J. Solid-State Circuits*, vol. 43, no. 12, pp. 2674–2692, 2008.
[13] T. Hong, M.-Z. Song, and Y. Liu, "Dual-Beam Directional Modulation Technique for Physical-Layer Secure Communication," *IEEE Antennas Wireless Propagat. Lett.*, vol. 10, pp. 1417–1420, 2011.
[14] Y. Ding and V. Fusco, "A Synthesis-Free Directional Modulation Transmitter Using Retrodirective Array," *IEEE J. Sel. Topics Signal Proc.*, vol. 11, no. 2, pp. 428–441, 2017.
[15] M. P. Daly and J. T. Bernhard, "Directional Modulation Technique for Phased Arrays," *IEEE Trans. Antennas. Propag.*, vol. 57, no. 9, pp. 2633–2640, 2009.
[16] Q. Zhu *et al.*, "Directional Modulation Based on 4-D Antenna Arrays," *IEEE Trans. Antennas. Propag.*, vol. 62, no. 2, pp. 621–628, 2014.
[17] N. Valliappan, A. Lozano, and R. W. Heath, "Antenna Subset Modulation for Secure Millimeter-Wave Wireless Communication," *IEEE Trans. Com.*, vol. 61, no. 8, pp. 3231–3245, 2013.
[18] N. N. Alotaibi and K. A. Hamdi, "Switched Phased-Array Transmission Architecture for Secure Millimeter-Wave Wireless Communication," *IEEE Trans. Com.*, vol. 64, no. 3, pp. 1303–1312, 2016.
[19] A. Kalantari *et al.*, "Directional Modulation Via Symbol-Level Precoding: A Way to Enhance Security," *IEEE J. Sel. Topics Signal Proc.*, vol. 10, no. 8, pp. 1478–1493, 2016.
[20] Q. Cheng *et al.*, "Time-Invariant Angle-Range Dependent Directional Modulation Based on Time-Modulated Frequency Diverse Arrays," *IEEE Access*, vol. 5, pp. 26 279–26 290, 2017.
[21] M. Hafez *et al.*, "Secure Spatial Multiple Access Using Directional Modulation," *IEEE Trans. Wirel. Com.*, vol. 17, no. 1, pp. 563–573, 2018.
[22] T. Xie, J. Zhu, and Y. Li, "Artificial-Noise-Aided Zero-Forcing Synthesis Approach for Secure Multi-Beam Directional Modulation," *IEEE Com. Lett.*, vol. 22, no. 2, pp. 276–279, 2018.
[23] F. Shu *et al.*, "Robust Secure Transmission of Using Main-Lobe-Integration-Based Leakage Beamforming in Directional Modulation MU-MIMO Systems," *IEEE Systems J.*, vol. 12, no. 4, pp. 3775–3785, 2018.

[24] ——, "Secure and Precise Wireless Transmission for Random-Subcarrier-Selection-Based Directional Modulation Transmit Antenna Array," *IEEE J. Selected Areas Com.*, vol. 36, no. 4, pp. 890–904, 2018.
[25] W.-Q. Wang and Z. Zheng, "Hybrid MIMO and Phased-Array Directional Modulation for Physical Layer Security in mmWave Wireless Communications," *IEEE J. Sel. Areas Com.*, vol. 36, no. 7, pp. 1383–1396, 2018.
[26] Y. Ding, V. Fusco, J. Zhang, and W.-Q. Wang, "Time-Modulated OFDM Directional Modulation Transmitters," *IEEE Trans. Vehicular Tech.*, vol. 68, no. 8, pp. 8249–8253, 2019.
[27] A. Narbudowicz, M. J. Ammann, and D. Heberling, "Directional Modulation for Compact Devices," *IEEE Antennas Wireless Propagat. Lett.*, vol. 16, pp. 2094–2097, 2017.
[28] J. Parron, E. A. Cabrera-Hernandez, A. Tennant, and P. de Paco, "Multiport Compact Stacked Patch Antenna With 360° Beam Steering for Generating Dynamic Directional Modulation," *IEEE Trans. Antennas. Propag.*, vol. 69, no. 2, pp. 1162–1167, 2021.
[29] A. Abu Arisheh *et al.*, "A Dynamic Pattern Dipole Antenna for Secure Wireless Communications," in *2022 IEEE Inter. Symposium Antennas Propag. and USNC-URSI*, 2022, pp. 1470–1471.
[30] A. Zandamela, N. Marchetti, and A. Narbudowicz, "Directional Modulation from a Wrist-Wearable Compact Antenna," in *2022 16th European Conference on Antennas and Propagation (EuCAP)*, 2022, pp. 1–5.
[31] A. Narbudowicz, A. Zandamela, N. Marchetti, and M. J. Ammann, "Energy-Efficient Dynamic Directional Modulation With Electrically Small Antennas," *IEEE Antennas Wireless Propagat. Lett.*, vol. 21, no. 4, pp. 681–684, 2022.
[32] H. Hamouda *et al.*, "Small Antenna embedded in a Wrist-Watch for Application in Telemedicine," in *European Conf. Antennas Propagat. (EuCAP)*, 2014, pp. 876–879.
[33] S.-W. Su and Y.-T. Hsieh, "Integrated Metal-Frame Antenna for Smartwatch Wearable Device," *IEEE Trans. Antennas. Propag.*, vol. 63, no. 7, pp. 3301–3305, 2015.
[34] Y.-S. Chen and T.-Y. Ku, "A Low-Profile Wearable Antenna Using a Miniature High Impedance Surface for Smartwatch Applications," *IEEE Antennas Wireless Propagat. Lett.*, vol. 15, pp. 1144–1147, 2016.
[35] D. Wu and S. W. Cheung, "A Cavity-Backed Annular Slot Antenna With High Efficiency for Smartwatches With Metallic Housing," *IEEE Trans. Antennas. Propag.*, vol. 65, no. 7, pp. 3756–3761, 2017.
[36] M. Jeon *et al.*, "GPS, Bluetooth and Wi-Fi tri-band antenna on metal frame of smartwatch," in *2016 IEEE Inter. Symposium Antennas Propag. (APSURSI)*, 2016, pp. 2177–2178.
[37] Y. Jia *et al.*, "Miniaturized wearable watch antenna for wristband applications," in *2019 IEEE MTT-S Inter. Microw. Biomedical Conference (IMBioC)*, vol. 1, 2019, pp. 1–3.
[38] M.-A. Chung, "Embedded 3D multi-band antenna with ETS process technology covering LTE/WCDMA/ISM band operations in a smart wrist wearable wireless mobile communication device design," *IET Microw. Antennas Propag.*, vol. 14, no. 1, pp. 93–100, 2020.
[39] S. Kumar *et al.*, "A Bandwidth-Enhanced Sub-GHz Wristwatch Antenna Using an Optimized Feed Structure," *IEEE Antennas Wireless Propagat. Lett.*, vol. 20, no. 8, pp. 1389–1393, 2021.
[40] B. Xiao *et al.*, "Design of Small Multiband Full-Screen Smartwatch Antenna for IoT Applications," *IEEE Internet Things J.*, vol. 8, no. 24, pp. 17 724–17 733, 2021.
[41] S. Woo *et al.*, "Design of a Compact UWB Diversity Antenna for WBAN Wrist-Watch applications," in *2013 Inter. Symposium Antennas Propag.*, vol. 02, 2013, pp. 1304–1306.
[42] W.-S. Chen *et al.*, "MIMO antenna with Wi-Fi and Blue-Tooth for smart watch applications," in *2015 IEEE MTT-S 2015 Inter. Microw. (IMWS-BIO)*, 2015, pp. 212–213.
[43] J. Chen *et al.*, "A multiple antenna system design for wearable device using theory of characteristic mode," in *European Conf. Antennas Propagat. (EuCAP)*, 2018, pp. 1–5.
[44] D. Wen *et al.*, "Design of a MIMO Antenna With High Isolation for Smartwatch Applications Using the Theory of Characteristic Modes," *IEEE Trans. Antennas. Propag.*, vol. 67, no. 3, pp. 1437–1447, 2019.
[45] B. Wang and S. Yan, "Design of smartwatch integrated antenna with polarization diversity," *IEEE Access*, vol. 8, pp. 123 440–123 448, 2020.
[46] C.-T. Liao, Z.-K. Yang, and H.-M. Chen, "Multiple Integrated Antennas for Wearable Fifth-Generation Communication and Internet of Things Applications," *IEEE Access*, vol. 9, pp. 120 328–120 346, 2021.
[47] L. Chen *et al.*, "An Efficient Directional Modulation Transmitter With Novel Crest Factor Reduction Technique," *IEEE Microw. Wirel. Components Lett.*, vol. 29, no. 8, pp. 554–556, 2019.
[48] J. M. Purushothama *et al.*, "Synthesis of Energy Efficiency Enhanced Directional Modulation Transmitters," *IEEE Trans. Green Com. Networks*, pp. 1–1, 2022.
[49] G. Huang, Y. Ding, and S. Ouyang, "Multicarrier Directional Modulation Symbol Synthesis Using Time-Modulated Phased Arrays," *IEEE Antennas Wireless Propagat. Lett.*, vol. 20, no. 4, pp. 567–571, 2021.
[50] J. Hou *et al.*, "Energy efficient time-modulated OFDM directional modulation transmitters," *Microw. Opt. Tech. Lett.*, vol. n/a, no. n/a, 2022.
[51] R. J. Maughan, J. S. Watson, and J. Weir, "The relative proportions of fat, muscle and bone in the normal human forearm as determined by computed tomography," *Clinical Science*, vol. 66, no. 6, pp. 683–689, 06 1984.
[52] C. Gabriel, "Compilation of the Dielectric Properties of Body Tissues at RF and Microwave Frequencies." Brooks Air Force Technical Report, AL/OE-TR-1996-0037, 1996.
[53] A. Zandamela, N. Marchetti, M. J. Ammann, and A. Narbudowicz, "Spherical Modes Driven Directional Modulation With a Compact MIMO Antenna," *IEEE Antennas Wireless Propagat. Lett.*, vol. 22, no. 3, pp. 477–481, 2023.
[54] J. E. Hansen, Ed., *Spherical Near-field Antenna Measurements*, ser. Electromagnetic Waves. Institution of Engineering and Technology, 1988. [Online]. Available: https://digital-library.theiet.org/content/books/ew/pbew026e